

GGRt: Towards Pose-free Generalizable 3D Gaussian Splatting in Real-time

Hao Li¹, Yuanyuan Gao¹, Dingwen Zhang¹, Chenming Wu², Yalun Dai³,
Chen Zhao², Haocheng Feng², Errui Ding², Jingdong Wang², and Junwei Han¹

¹ Brain and Artificial Intelligence Lab, Northwestern Polytechnical University
lifugan_10027@outlook.com, zhangdingwen2006yyy@gmail.com
yyg7645@gmail.com, junweihan2010@gmail.com

² Department of Computer Vision, Baidu Inc. {wuchenming, zhaochen03,
fenghaocheng, dingerrui, wangjingdong}@baidu.com

³ Nanyang Technological University daiy0018@e.ntu.edu.sg

Abstract. This paper presents GGRt, a novel approach to generalizable novel view synthesis that alleviates the need for real camera poses, complexity in processing high-resolution images, and lengthy optimization processes, thus facilitating stronger applicability of 3D Gaussian Splatting (3D-GS) in real-world scenarios. Specifically, we design a novel joint learning framework that consists of an Iterative Pose Optimization Network (IPO-Net) and a Generalizable 3D-Gaussians (G-3DG) model. With the joint learning mechanism, the proposed framework can inherently estimate robust relative pose information from the image observations and thus primarily alleviate the requirement of real camera poses. Moreover, we implement a deferred back-propagation mechanism that enables high-resolution training and inference, overcoming the resolution constraints of previous methods. To enhance the speed and efficiency, we further introduce a progressive Gaussian cache module that dynamically adjusts during training and inference. As the first pose-free generalizable 3D-GS framework, GGRt achieves inference at ≥ 5 FPS and real-time rendering at ≥ 100 FPS. Through extensive experimentation, we demonstrate that our method outperforms existing NeRF-based pose-free techniques in terms of inference speed and effectiveness. It can also approach the real pose-based 3D-GS methods. Our contributions provide a significant leap forward for the integration of computer vision and computer graphics into practical applications, offering state-of-the-art results on LLFF, KITTI, and Waymo Open datasets and enabling real-time rendering for immersive experiences.

Keywords: Pose-Free · Generalizable 3D-GS · Real-time Rendering

1 Introduction

Recently invented Neural Radiance Fields (NeRF) [18] and 3D Gaussian Splatting (3D-GS) [11] bridge the gap between computer vision and computer graphics in the tasks of image-based novel view synthesis and 3D reconstruction. With

a variety of follow-up variants, they are rapidly pushing the boundary towards revolutionizing many areas, such as virtual reality, film production, immersive entertainment, etc. To enhance generalization capabilities across previously unseen scenes, recent developments have introduced innovative approaches such as the generalizable NeRF [27] and 3D-GS [2].

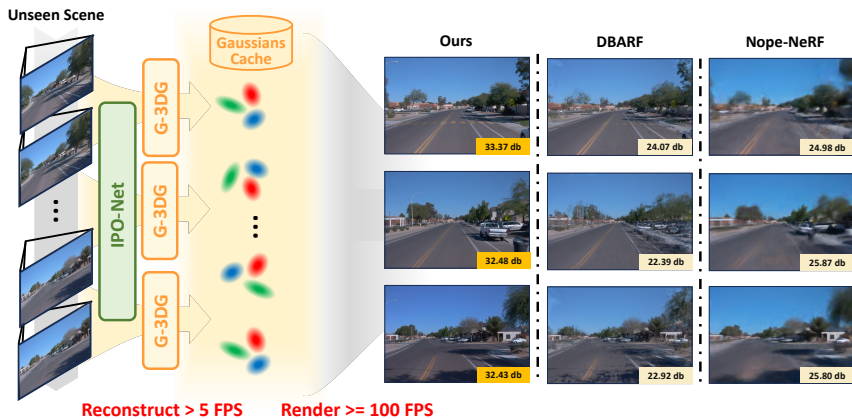


Fig. 1: Our proposed GGRt stands for the first pose-free generalizable 3D Gaussian splatting approach, capable of inference at over 5 FPS, and delivering real-time rendering performance.

Despite their ability to reconstruct new scenes without optimization, the previous works usually rely on the actual camera pose for each image observation, which actually cannot always be captured accurately in real-world scenarios. Besides, these methods show unsatisfactory view synthesis performance and struggle to reconstruct at higher resolutions due to the large number of parameters used. Last but not least, for such methods, each time when synthesizing a novel view demands a complete forward pass of the whole network, making real-time rendering intractable.

To tackle these challenges, this paper proposes GGRt, which brings the benefits of a primitive-based 3D representation—fast and memory-efficient rendering—to the generalizable novel view synthesis under the pose-free condition. Specifically, we introduce a novel pipeline that jointly learns the IPO-Net and the G-3DG model. Such a pipeline can estimate relative camera pose information robustly and thus effectively alleviate the requirement for real camera poses. Subsequently, we develop a deferred back-propagation (DBP) mechanism, allowing our method to efficiently perform high-resolution training and inference, a capability that surpasses the low-resolution limitations of existing methods [9, 12, 20, 26]. Furthermore, we also design an innovative Gaussians cache module with the idea of reusing the relative pose information and image features of the reference views in two continuous training and inferencing iterations. Thus, the Gaussians cache can progressively grow and diminish throughout the training and inferencing processes, further accelerating the speed of both.

To the best of our knowledge, our work stands for the first pose-free generalizable 3D Gaussian splatting, inference at ≥ 5 FPS, and rendering in real-time at ≥ 100 FPS. Extensive experiments demonstrate that our method surpasses existing NeRF-based pose-free approaches in inference speed and effectiveness. Compared to pose-based 3D-GS methods, our approach provides faster inference and competitive performance, even without the camera pose prior.

2 Related Work

2.1 Generalizable Novel View Synthesis

Pioneering approaches involving novel view synthesis leverage image-based rendering techniques, such as light field rendering [21,23] and view interpolation [27,32]. The introduction of NeRF [18] marks a significant milestone that uses neural networks to model the volume scene function and demonstrates impressive results in this task but requires per-scene optimization and accurate camera poses. To address the problem of generalization, researchers have explored several directions. For instance, PixelNeRF [34] presents a NeRF architecture that is conditioned on image inputs in a fully convolutional fashion. NeuRay [15] enhances the NeRF framework by predicting the visibility of 3D points relative to input views, allowing the radiance field construction to concentrate on visible image features. Furthermore, GNT [27] integrates multi-view geometry into an attention-based representation, which is then decoded through an attention mechanism in the view transformer for rendering novel views.

A recent work LRM [10] and its multi-view version [13], also adopt a transformer for generalizable scene reconstruction using either a single image or posed four images. However, those works only demonstrate the capability in object-centric scenes, while our work targets a more ambitious goal of being generalizable in both indoor and outdoor scenes. Fu et al. [4] propose to use a generalizable neural field from posed RGB images and depth maps, eschewing a fusion module. Our work, in contrast, requires only camera input without pose information.

The aforementioned works use implicit representation inherited from NeRF and its variants, showing slow training and inferencing speed. Differently, pixelSplat [2] is the first generalizable 3D-GS work that tackles the problem of synthesizing novel views between a pair of images. However, it still requires accurate poses and only supports a pair of images as inputs. Instead, our work dismisses the demand for image poses and supports large-scale scene inference with unlimited images as reference views.

2.2 Pose-free Modeling for Novel View Synthesis

The first attempt towards pose-free novel view synthesis is iNeRF [33], which uses key-point matching to predict camera poses. NeRF- [31] proposes to optimize camera pose embeddings and NeRF jointly. [14] proposes to learn neural 3D representations and register camera frames using coarse-to-fine positional encodings. [1] integrates scale and shift-corrected monocular depth priors to train their

model, enabling the joint acquisition of relative poses between successive frames and novel view synthesis of the scenes. [16] employs a strategy that synergizes pre-trained depth and optical-flow priors. This approach is used to progressively refine blockwise NeRFs, facilitating the frame-by-frame recovery of camera poses.

The implicit modeling inherent to NeRF complicates the simultaneous optimization of scene and camera poses. However, the recent innovation of 3D-GS provides an explicit point-based scene representation, enabling real-time rendering and highly efficient optimization. A recent work [5] pushes the boundary of simultaneous scene and pose optimization. However, those approaches need tremendous efforts in training and optimization per scene.

In generalizable settings, SRT [19], VideoAE [12], RUST [20], MonoNeRF [26], DBARF [3] and FlowCam [22] learn a generalizable scene representation from unposed videos using NeRF’s implicit representation. Those works show unsatisfactory view synthesis performance without per-scene optimization and inherent all the drawbacks NeRF originally had, such as real-time rendering of explicit primitives. PF-LRM [28] extends LRM to be applicable in pose-free scenes by using a differentiable PnP solver, but it shows the same limitations of LRM [10] mentioned above. To the best of our knowledge, our work stands for the first pose-free generalizable 3D-GS that enables efficient inferencing and real-time rendering, exhibiting SOTA performance in various metrics compared to previous approaches.

3 Our Approach

Given N unposed images $\mathbb{I} = \{\mathbf{I}_r \in \mathbb{R}^{H \times W \times 3} \mid r = 1 \dots N\}$ as references, our goal is to synthesize target (or called query) image $\mathbf{I}_t \in \mathbb{R}^{H \times W \times 3}$ from novel view with corresponding poses $\mathbb{T} = \{\mathbf{T}_{r \rightarrow t} \mid r = 1 \dots N\}$. Our GGRT is designed to train a generalizable Gaussian splatting network in a self-supervised manner, without relying on any camera pose or depth acquired in advance.

3.1 The Joint Learning Framework

Shared Image Encoder. We utilize the ResNet backbone pre-trained with DINO and augmented with feature pyramid networks (FPN) to extract both geometric and semantic cues from each reference view \mathbf{I}_r and the target view \mathbf{I}_t . The extracted features are denoted as \mathbf{F}_r and \mathbf{F}_t .

Iterative Pose Optimization Network. The goal of our pose estimation is to obtain the relative pose $\mathbf{T}_{r \rightarrow t}$ between target and reference images. Hence the target image can be aggregated by the reference images. To this end, an intuitive solution is to build a cost function \mathcal{C} that enforces the feature-metric consistency across the target view and all nearby views (*i.e.* minimize the re-projection error):

$$\mathcal{C} = \frac{1}{|\mathcal{N}(t)|} \sum_{r \in \mathcal{N}(t)} \|\chi(\mathbf{T}_{r \rightarrow t} \mathbf{D}_t, \mathbf{F}_r) - \chi(\mathbf{u}_t, \mathbf{F}_t)\|, \quad (1)$$

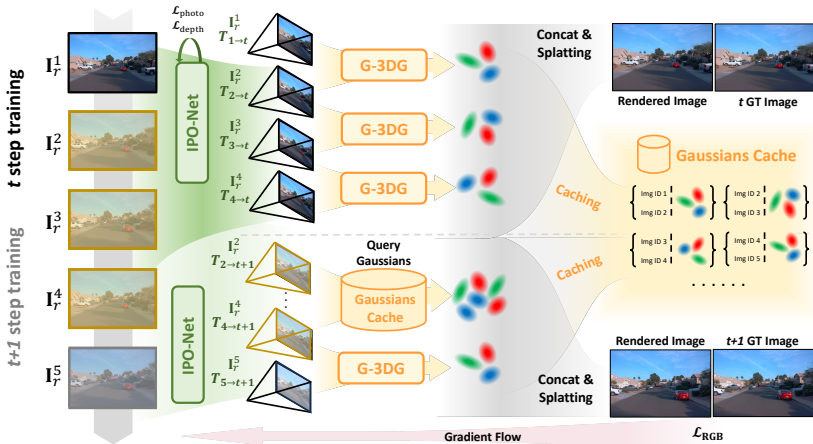


Fig. 2: An overview of our method, demonstrated by using two continuous training steps given N selected nearby images. In the first training step, reference views are selected from nearby time $r \in \mathcal{N}(t)$, then the IPO-Net estimates the relative poses between reference and target image $\mathbf{T}_{r \rightarrow t}$ for 3D-Gaussian predictions. Then $\mathbf{I}_r^1 \cdots \mathbf{I}_r^4$ forms three image pairs and is fed into the G-3DG model to predict Gaussians $\mathbf{G}_1 \cdots \mathbf{G}_3$ for novel view splatting and store them in Gaussians cache. In the second step, since $\mathbf{I}_r^2 \cdots \mathbf{I}_r^4$ are collaboratively used by the last step, we directly query their image ID in the Cache Gaussians and pick up corresponding Gaussian points $\mathbf{G}_2, \mathbf{G}_3$ with newly predicted \mathbf{G}_4 for novel view splatting.

where χ denotes the interpolation function (e.g., bilinear interpolation), and \mathbf{D}_t is the predicted depth of the target image. Afterward, following the RAFT [25] architecture, we adopt a Conv-GRU module to iterative update the camera pose $\mathbf{T}_{r \rightarrow t}$ and depth map \mathbf{D}_t . Specifically, at the iteration step $k = 0$, given camera poses $\mathbf{T}_{r \rightarrow t}^{k=0}$ and depth map $\mathbf{D}_t^{k=0}$, we compute an initial cost map $C^{k=0}$ using Eq. 1. Then, the Conv-GRU module predicts the relative camera pose difference $\Delta \mathbf{T}_{r \rightarrow t}$ and depth difference $\Delta \mathbf{D}_t$ to update the camera poses and the depth map for a predefined maximal number of iterations K , such that:

$$\mathbf{T}_{r \rightarrow t}^{(k)} = \mathbf{T}_{r \rightarrow t}^{(k-1)} + \Delta \mathbf{T}_{r \rightarrow t}, \quad \mathbf{D}_t^{(k)} = \mathbf{D}_t^{(k-1)} + \Delta \mathbf{D}_t. \quad (2)$$

Then we transfer our pre-estimated relative poses $\mathbf{T}_{r \rightarrow t}$ between reference views and target view to relative poses $\mathbf{T}_{r \rightarrow r+1}$ between nearby references view for our Gaussians prediction. We denote the network as IPO-Net in the following context.

Generalizable 3D-Gaussians. Unlike previous generalizable methods that rely on implicit neural rendering and require ray aggregation for each target view, our approach is based on 3D-GS, which employs an explicit representation. As a result, we can generate Gaussian points from reference views and combine them to render a larger scene. To accomplish this, we organize the image set \mathbb{I} into several image pairs as well as their relative poses $\{(\mathbf{I}_r^1, \mathbf{I}_r^2, \mathbf{T}_{1 \rightarrow 2}), \dots, (\mathbf{I}_r^{N-1}, \mathbf{I}_r^N, \mathbf{T}_{N-1 \rightarrow N})\}$

and perform pixel-aligned Gaussian prediction $\mathbf{G}_i = \{\mathbf{g}_k = (\boldsymbol{\mu}_k, \boldsymbol{\Sigma}_k, \boldsymbol{\alpha}_k, \mathbf{S}_k)\}_k^K$ for each image pair $(\mathbf{I}_r^i, \mathbf{I}_r^{i+1})$.

In particular, given an image pair $(\mathbf{I}_r^i, \mathbf{I}_r^{i+1})$, we design a module dubbed Generalizable 3D-Gaussians(G-3DG) to predict Gaussian points, which consists of three parts: 1) Epipolar Sampler, 2) Cross-Attention module, and 3) Local Self-Attention module. Let \mathbf{u}^i be the pixel coordinate from \mathbf{F}_r^i and ℓ be the epipolar line induced by its ray in \mathbf{F}_r^{i+1} . First, along ℓ , we sampled the features $\mathbf{F}_r^{i+1}[\mathbf{u}_\ell^{i+1}]$ and the annotated points in it with the corresponding depths \mathbf{D}_ℓ^{i+1} :

$$S(\mathbf{F}_r^{i+1}) = \mathbf{F}_r^{i+1}[\mathbf{u}_\ell^{i+1}] \oplus \mathcal{PE}(\mathbf{D}_\ell^{i+1}), \quad (3)$$

where \oplus and $\mathcal{PE}(\cdot)$ indicates concatenation and positional encoding. Subsequently, we employ the Cross-Attention module $\mathcal{CA}(\cdot)$ to determine per-pixel correspondence. The feature $\hat{\mathbf{F}}_i$ incorporates a weighted sum of the depth positional encoding, with the expectation that the highest weight corresponds to the correct correspondence.

$$\hat{\mathbf{F}}_r^i = \mathbf{F}_r^i + \mathcal{CA}(q = \mathbf{F}_r^i, k = S(\mathbf{F}_r^{i+1}), v = S(\mathbf{F}_r^{i+1})). \quad (4)$$

Furthermore, we use a self-attention module to ensure our network propagates scaled depth estimation to part of the i -th image feature maps that may not have any epipolar correspondences in the $(i+1)$ -th image. For high-resolution novel view synthesis, we separate a high-resolution image into several small crops and utilize a Local Self-Attention module $\mathcal{LSA}(\cdot)$. This way, we can keep the training objective the same as the global self-attention trained on full images. In detail, we split features \mathbf{F}_r^i into $M \times M$ patches and conduct self-attention ($\mathcal{SA}(\cdot)$) for every patch. Then, we add positional encoding $\mathcal{PE}(H, W)$ to retain the image-wise positional information, where H and W denote the height and width of the features \mathbf{F}^i .

$$\tilde{\mathbf{F}}_r^i = \mathcal{LSA}(\hat{\mathbf{F}}_r^i) = \hat{\mathbf{F}}_r^i + \begin{bmatrix} \mathcal{SA}(\hat{\mathbf{F}}_{r,1,1}^i) & \mathcal{SA}(\hat{\mathbf{F}}_{r,1,2}^i) & \cdots & \mathcal{SA}(\hat{\mathbf{F}}_{r,1,m}^i) \\ \mathcal{SA}(\hat{\mathbf{F}}_{r,2,1}^i) & \mathcal{SA}(\hat{\mathbf{F}}_{r,2,2}^i) & \cdots & \mathcal{SA}(\hat{\mathbf{F}}_{r,2,m}^i) \\ \vdots & \vdots & \ddots & \vdots \\ \mathcal{SA}(\hat{\mathbf{F}}_{r,m,1}^i) & \mathcal{SA}(\hat{\mathbf{F}}_{r,m,2}^i) & \cdots & \mathcal{SA}(\hat{\mathbf{F}}_{r,m,m}^i) \end{bmatrix} + \mathcal{PE}(H, W). \quad (5)$$

Upon $\tilde{\mathbf{F}}_r^i$, we predict its corresponding Gaussian points \mathbf{G}_i following the implementation of pixelSplat [2]. Our proposed training strategy naturally enables us to concatenate all the Gaussian points generated by image pairs for large scene generalization:

$$\mathbb{G} = \{\mathbf{G}_1, \mathbf{G}_2, \dots, \mathbf{G}_{N-1}\}. \quad (6)$$

Moreover, our approach can achieve comparable performance while significantly reducing the required time for encoding reference images and therefore facilitating real-time rendering.

Gaussians Cache Mechanism. As shown in Fig. 2, for two continuous training/inferencing iterations, many reference views \mathbf{I}_r^i of the current iteration are

co-used by the last iteration. Re-inferencing them in the next iteration will be time-consuming and unnecessary since they share the same relative pose and features. Therefore, instead of re-predicting Gaussian points for all image pairs, we propose a dynamic store, query, and release mechanism called Gaussians Cache. In t -th step, it stores the predicted Gaussian points with corresponding image IDs $\{i : \mathbf{G}_i\}$ in the cache. In $(t + 1)$ -th step, it queries the Cache using image ID i to restore the Gaussian points \mathbf{G}_i . Furthermore, after querying all the IDs in the current iteration, the Cache releases the remaining unmatched Gaussians to optimize memory usage. This ensures that these Gaussians will not be utilized in the future, thereby reducing memory footprint without compromising performance.

3.2 End-to-end Training with Deferred Optimization

Jointly Training Strategy. Learning scenes without camera pose is challenging due to the lack of 3D spatial priors to learn potential occlusions, varying lighting conditions, and the camera intrinsics encountered in unstructured environments. To address this problem, as depicted in Figure 2(b), we activate the gradients of both the IPO-Net and G-3DG model, allowing for their simultaneous learning. By leveraging supervision from our rendered images, we can effectively optimize our IPO-Net.

Specifically, to strike a balance between pose estimation and training a generalized Gaussian network, we employ joint training of our GGRT model using the loss function $\mathcal{L}_{\text{joint}}$, which incorporates dynamic weight coefficient adjustment:

$$\mathcal{L}_{\text{joint}} = 2^{\beta \cdot t} (\mathcal{L}_{\text{depth}} + \mathcal{L}_{\text{photo}}) + (1 - 2^{\beta \cdot t}) \mathcal{L}_{\text{rgb}}, \quad (7)$$

where t denotes the training step. For IPO-Net optimization, we adopt photometric loss $\mathcal{L}_{\text{photo}}$ [8] and edge-aware smoothness $\mathcal{L}_{\text{depth}}$ [7] for our target view:

$$\mathcal{L}_{\text{photo}} = \frac{1}{|\mathcal{N}_t|} \sum_{r \in \mathcal{N}_t} \left(\alpha \frac{1 - \text{ssim}(\mathbf{I}'_t - \mathbf{I}_t)}{2} + (1 - \alpha) \|\mathbf{I}'_t - \mathbf{I}_t\| \right), \quad (8)$$

$$\mathcal{L}_{\text{depth}} = |\partial_x \mathbf{D}| \exp^{-|\partial_x \mathbf{I}|} + |\partial_y \mathbf{D}| \exp^{-|\partial_y \mathbf{I}|}, \quad (9)$$

where \mathbf{I}'_t denotes the warped image from the reference view r to target view t . ∂_x and ∂_y are the image gradients. For our Gaussian model training, we simply apply MSE error between the rendered target image $\hat{\mathbf{C}}$ and the ground truth target image \mathbf{C} , where \mathbf{u} denotes pixel coordinate from image \mathbf{I}_t :

$$\mathcal{L}_{\text{rgb}} = \sum_{\mathbf{u} \in \mathbf{u}} \left\| \hat{\mathbf{C}}(\mathbf{u}) - \mathbf{C}(\mathbf{u}) \right\|_2^2. \quad (10)$$

Deferred Back-propagation for Generalizable Gaussians. One of our goals is to render high-resolution images at a fast speed. However, with the growing image size, there will be insufficient memory to train a full high-resolution

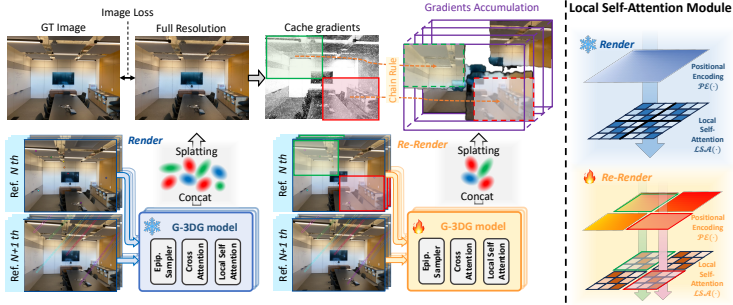


Fig. 3: Illustration of deferred back-propagation pipeline of our G-3DG model (left column) and the procedure of our local self-attention module in deferred back-propagation (right column). Details are shown in Sec. 3.2.

image due to the limited GPU memory. Inspired by [35], as shown in Fig. 3, we specifically design *deferred back-propagation* with G-3DG model that allows us to train GGRt in a high resolution under memory constraints. Specifically, we generate a full-resolution image during the initial stage without utilizing auto-differentiation. Subsequently, we compute the image loss and its gradient on a per-pixel basis with regard to the rendered image. During the second stage, we adopt a patch-wise approach to re-render pixels, enabling auto-differentiation. This allows us to back-propagate the cached gradients to the network parameters, facilitating their accumulation.

As mentioned earlier, the crucial aspect of ensuring successful training in the technique is maintaining consistency in our training objective across the two stages. Employing traditional self-attention mechanisms for both the entire image and patch images would result in an imbalance, as the features in the whole image can globally attend to information. In contrast, patch images can only focus on one patch at a time. To solve this problem, for every image pair $(\mathbf{I}_r^i, \mathbf{I}_r^{i+1})$ in N reference images, we split the \mathbf{I}_r^i into $M \times M$ patches $[\mathbf{I}_{1,1}^i, \dots, \mathbf{I}_{m,m}^i]$, each patch follows the same shape with Local Self-Attention module elaborated above. For each patch $\mathbf{I}_{m,m}^i$, we rewrite the epipolar sampler of Eq. 3 as:

$$S(\mathbf{F}_r^{i+1}) = \mathbf{F}_r^{i+1}[\mathbf{u}_{\ell^{m,m}}^{i+1}] \oplus \gamma(d_{\ell^{m,m}}^{i+1}) \quad (11)$$

where $\ell^{m,m}$ denotes the epipolar lines induced by patch $\mathbf{I}_{m,m}^i$. During the Cross-Attention module, we replace q from \mathbf{F}_r^i to $\mathbf{F}_{m,m}^i$ in Eq. 4, which aims to aggregate global features from \mathbf{F}_{i+1}^s for each pixel:

$$\mathbf{F}_{m,m}^i = \mathbf{F}_{m,m}^i + \mathcal{CA}(q = \mathbf{F}_{m,m}^i, k = S(\mathbf{F}_r^{i+1}), v = S(\mathbf{F}_r^{i+1})) \quad (12)$$

As for the self-attention module, firstly, we keep the positional encoding in global image-wise and crop them using the patch position to retain positional information between different patches. After that, the self-attention block $\mathcal{SA}(\cdot)$ is adopted for our patch feature $\mathbf{F}_{m,m}^i$:

$$\mathbf{F}_{m,m}^i = \mathbf{F}_{m,m}^i + \mathcal{SA}(\mathbf{F}_{m,m}^i) + \text{Crop}(\mathcal{PE}(H, W), m, m) \quad (13)$$

This design allows us to achieve consistent results between full image rendering and deferred rendering.

3.3 Efficient Rendering

By generating pixel-aligned Gaussian points in the reference views without being constrained by a specific target view, we can decompose the Gaussian generation process and the novel view splatting process. This decomposition enables us to render real-time at a high frame rate (≥ 100 FPS). During practical implementation, we generate and cache all the Gaussian points in the scene (*i.e.* Gaussians Cache). As a result, when presented with a query view within the scene, we can efficiently retrieve the corresponding Gaussians by utilizing the nearby reference images’ IDs. This allows us to render a novel view quickly and accurately.

4 Experiments

4.1 Implementation Details

The experiments for novel view synthesis are conducted under two settings, *i.e.*, the *generalized* and *finetuned* settings. Firstly, we train our model in several scenes and directly evaluate our model on test scenes (*i.e.*, unseen scenes). Secondly, we finetune our generalized model on each unseen scene with a small number of steps and compare them with per-scene optimized NeRF methods.

Datasets. Following [3], we train and evaluate our method on LLFF [17]. To further demonstrate the capability of our model in general settings, we evaluate our performance in forward-facing outdoor datasets (*i.e.* Waymo Open Dataset [24] and KITTI Dataset [6]).

Parameters. We train our method end-to-end on datasets of multi-view unposed images using the Adam optimizer to minimize the overall loss \mathcal{L}_{all} . The learning rates set for IPO-Net and G-3DG model are 5×10^{-4} and 2×10^{-5} respectively, decaying exponentially over the course of training. For the LLFF dataset, our training and rendering resolutions are set to 378×504 . The number of reference views is 5 for the generalized setting and 10 for the finetuning setting. As for the Waymo dataset, the rendering resolution is set to 640×960 for both generalized and finetuning settings. The training resolutions are set to 196×288 and 504×760 respectively. For the KITTI dataset, we train and render with the same resolution 176×612 . The number of reference views is set to 5 for both the generalized and finetuning settings. We split our training images into 4 patches during deferred back-propagation.

Metrics. For render quality evaluation, Peak Signal-to-Noise Ratio (PSNR), Structural Similarity Index Measure (SSIM) [30], and the Learned Perceptual Image Patch Similarity (LPIPS) [36] are adopted.

Table 1: Quantitative performance of novel view synthesis on the Waymo [24] and LLFF [17] datasets under generalized conditions. Entries in **bold** indicate the best performance in a pose-free context, while **highlighted** represents the best overall.

Scene	PSNR \uparrow				SSIM \uparrow				LPIPS \downarrow				
	Pose-free \times		Pose-free \checkmark		Pose-free \times		Pose-free \checkmark		Pose-free \times		Pose-free \checkmark		
	IBRNet	PixelSplat	DBARF	Ours	IBRNet	PixelSplat	DBARF	Ours	IBRNet	PixelSplat	DBARF	Ours	
Waymo	003	31.40	31.45	25.17	31.20	0.917	0.920	0.834	0.912	0.127	0.101	0.225	0.137
	19	30.06	32.22	23.45	32.34	0.907	0.928	0.810	0.928	0.130	0.082	0.225	0.110
	36	29.88	33.58	22.59	31.64	0.904	0.942	0.807	0.919	0.150	0.087	0.254	0.120
	69	30.24	31.81	21.97	32.10	0.889	0.914	0.779	0.908	0.175	0.119	0.307	0.146
	81	31.30	31.02	24.17	31.30	0.901	0.904	0.785	0.892	0.147	0.108	0.298	0.159
	126	36.00	33.68	29.70	34.15	0.940	0.931	0.884	0.937	0.106	0.100	0.178	0.094
	LLFF	fern	23.61	22.90	23.12	24.66	0.743	0.734	0.724	0.764	0.240	0.121	0.277
flower		22.92	24.51	21.89	24.80	0.849	0.806	0.793	0.795	0.123	0.106	0.176	0.098
fortress		29.05	26.36	28.13	28.30	0.850	0.781	0.820	0.817	0.087	0.080	0.126	0.109
horns		24.96	23.86	24.17	26.34	0.831	0.836	0.799	0.872	0.144	0.127	0.194	0.118
leaves		19.03	19.49	18.85	21.03	0.737	0.663	0.649	0.729	0.289	0.158	0.313	0.150
orchids		18.52	17.65	17.78	19.00	0.573	0.533	0.506	0.589	0.259	0.191	0.352	0.219
room		28.81	27.82	27.50	29.02	0.926	0.920	0.901	0.932	0.099	0.067	0.142	0.081
trex		23.51	22.75	22.70	24.22	0.818	0.788	0.783	0.804	0.160	0.107	0.207	0.166

Table 2: Results for novel view synthesis on KITTI [6] dataset in generalized settings. Specifically, ‘w/o ft’ denotes applying our method directly on KITTI using the weights trained on the Waymo dataset without finetuning, whereas ‘w/ ft’ denotes the results from our model finetuned on KITTI in scene ‘04’. Resolution is 176×612 . Time includes inferencing and rendering.

Metric	Pose-free \times		Pose-free \checkmark					
	IBRNet	PixelSplat	VideoAE	RUST	FlowCAM	DBARF	Ours w/o ft	Ours w/ ft
PSNR \uparrow	22.5	23.35	15.17	14.18	17.69	18.36	20.24	22.59
LPIPS \downarrow	0.44	0.129	0.462	0.654	0.405	0.425	0.388	0.327
Time(s) \downarrow	0.850	0.285	≈ 2	≈ 1	4.170	0.850	0.295	0.295

4.2 Benchmarking

We first conduct experiments to compare our method with other methods, including both pose-required and pose-free, in light field dataset, LLFF [17] and forward-facing autonomous driving dataset, Waymo Open dataset [24]. As shown in Tab. 1, our method achieves remarkable performance improvements compared to other approaches. Notably, our method comprehensively surpasses the best pose-free method DBARF [3], across all scenarios in both datasets. Specifically, in the ‘69’ scene of the Waymo dataset, our method’s PSNR exceeds that of DBARF by up to 10.3 dB. Furthermore, compared to state-of-the-art pose-based methods like IBRNet [29] and pixelSplat [2], our method also delivers highly competitive results. For instance, our method outperforms IBRNet and pixelSplat in most scenarios on the LLFF dataset. In the ‘horns’ scene, our approach achieves a PSNR of 1.38 dB and 2.48 dB higher than IBRNet and pixelSplat, respectively.

We also conduct experiments on the KITTI [6] dataset to compare our method with other pose-free generalizable NeRF methods. As illustrated in Tab. 2, our approach outperforms the VideoAE [12], RUST [20], and FlowCAM [22], even without specifically training on the KITTI dataset. Notably, when we directly apply our Waymo-trained model to KITTI without any additional training, our method still surpasses those approaches that have been

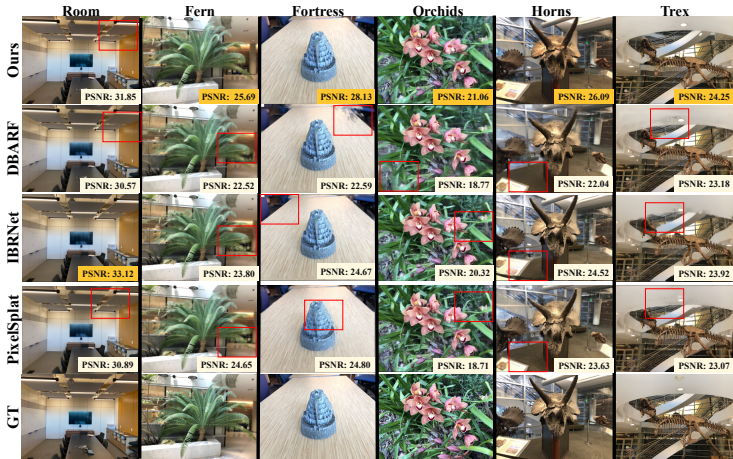


Fig. 4: Novel view synthesis qualitative outcomes on the LLFF [17] dataset under generalized settings, with significant regions highlighted by red rectangles.

specifically trained on KITTI. Through fine-tuning our method on the KITTI dataset, we observe even more significant improvements. The PSNR values reach a remarkable value of 22.59 dB, surpassing the state-of-the-art method FlowCAM by a substantial margin of 4.9 dB.

Pose Accuracy Evaluation. We assess the accuracy of our pose estimation on both quantitative and qualitative levels. Since we focus on estimating relative poses rather than absolute poses, we compare our results exclusively with DBARF. The comparison results are presented in Tab. 3, where we achieve better rotation and translation errors in most of the scenes. Notably, our rotation errors are significantly lower in the ‘Flower’ and ‘Trex’ scenes, consequently bringing significant reconstruction quality improvement by 2.91dB and 1.52dB in PSNR.

4.3 Ablation Study

Effectiveness of Gaussians Cache. In this ablation study, we compare our method’s training and inferencing time consumption on a single RTX 3090 GPU

Table 3: Quantitative results of camera pose accuracy on LLFF [17] dataset. Rotation denotes degree and translation is scaled by 10^2 .

Error	Method	Room	Trex	Flower	Fern	Fortress	Orchids	Leaves	Horns
Rotation↓	DBARF	9.590	126.93	14.650	8.314	2.740	14.43	13.927	8.455
	Ours	7.692	3.449	5.885	5.783	2.160	4.157	16.964	4.684
Translation↓	DBARF	0.060	0.070	0.010	0.020	0.009	0.046	0.022	0.027
	Ours	0.043	0.014	0.004	0.008	0.006	0.012	0.014	0.005

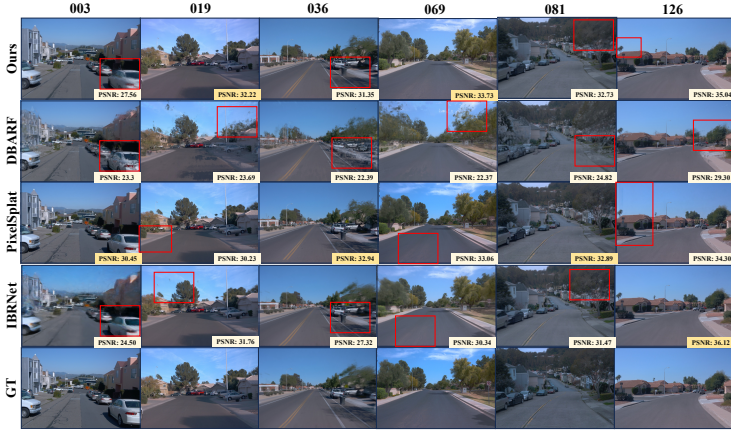


Fig. 5: Qualitative results for novel view synthesis on Waymo [24] dataset with generalized settings. Areas of distinction are marked with red rectangles.

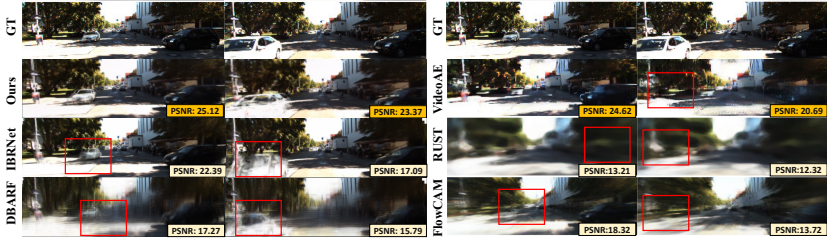


Fig. 6: Results of novel view synthesis on the KITTI [6] dataset under generalized conditions, with red rectangles indicating areas of note. Note that ground truth (GT) is replicated for easier comparison.

Table 4: Ablation study evaluating the proposed Gaussians Cache mechanism. Training&inference conducted on Waymo ‘019’ dataset with a resolution of 228×320 .

Gaussians Cache	Training Time↓	Inference Time↓	PSNR↑
✗	4s/iter	1.02s/iter	32.34
✓	2s/iter	0.13s/iter	32.34

and further evaluate its impact on the metric of PSNR. As shown in Tab. 4, the proposed Gaussians Cache prevents the need for re-predicting Gaussians that were processed in the previous iteration, resulting in a $2\times$ speed increase during training and $8\times$ boost during inference when compared to the baseline without Gaussians cache. Additionally, the proposed caching technique has been shown to have no negative impact on performance, underscoring its efficacy.

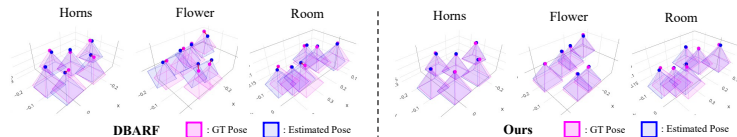


Fig. 7: Qualitative results for pose optimization on three scenes of LLFF [17] dataset.



Fig. 8: Visualization of our method and crop image training. (a) Individual image patches are rendered separately and stitched together. (b) The entire image is rendered using the weights trained with our crop image training approach. (c) The entire image is rendered using our deferred back-propagation technique.

Effectiveness of Deferred Back-Propagation. We evaluate the performance influence of the proposed DBP technique. As shown in Tab. 5, when using the regular back-propagation, a single RTX 3090 GPU can only process 2 reference views with the resolution of 384×496 . If we want to use more reference views, we need to reduce the resolution of the observed images, which would bring undesired performance drops. However, when equipped with the proposed DBP technique, we can use 5 reference views with the resolution of 384×496 and gain 1.37 – 3.02 dB in PSNR compared to the traditional approach. The performance gains become even more under the finetune setting. Notably, when continually increasing the number of reference views to 7, our approach reaches 31.5 dB in PSNR, setting a new state-of-the-art record.

Apart from DBP, a simple idea to train a high-resolution model with limited hardware is to crop images from reference views randomly and only render the cropped areas. We compared the training strategy with the Crop Image strategy and our DBP. After training the model with cropped images, it fails to capture the matching information of the entire image, resulting in poor rendering results when directly using a full image, which will. On the contrary, our proposed DBP works well under this circumstance as shown in Fig. 8.

Effectiveness of Local Self-Attention. Here we conduct ablations of our proposed local self-attention. As shown in Fig. 9(a), without our local self-attention, the rendered images between the first and second steps of DBP are not consistent. Specifically, without the inclusion of Local Self-Attention, the PSNR performance experiences a drop after around 1,500 training steps, as illustrated in Fig. 9 (b). To our knowledge, by utilizing Local Self-Attention, the results of

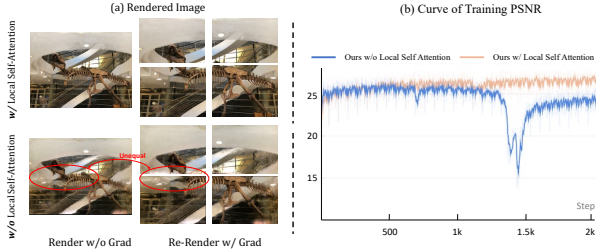


Fig. 9: Ablation of our Local Self Attention for DBP. Left: the top and bottom row demonstrate the visualization of our DBP w/ or w/o local self-attention. ‘Render w/o Grad’ denotes the full image ; Right: the PSNR over the course of training, a significant drop can be observed without our Local Self Attention.

Table 5: Ablation study of our proposed deferred back-propagation technique on Scene ‘ROOM’ from the LLFF dataset [17]. ‘OOM’ is an abbreviation for ‘out of memory’.

Method	Ref. View Resolution		PSNR \uparrow		Mem. (GB)	
	Gen.	Ft	Gen.	Ft	Gen.	Ft
Our <i>w/o</i> Defer	2	384×496	27.65	27.77	28.48	29.03
Our <i>w/o</i> Defer	3	384×496	-	-	OOM	OOM
Our <i>w/o</i> Defer	5	192×248	26.00	28.51	31.05	31.05
Our <i>w/</i> Defer	5	384×496	29.02	29.85	29.35	29.35
Our <i>w/</i> Defer	7	384×496	-	31.50	-	34.61

both processes remain consistent. Otherwise, the loss calculated by the forward-only rendering process no longer serves as an appropriate guide for the gradient backpropagation of the DBP rendering process, resulting in a significant decrease in PSNR.

5 Conclusion

This paper introduces a novel method for generalizable novel view synthesis that eliminates the need for camera poses, enables high-resolution real-time rendering, and eliminates lengthy optimization. Our method contains jointly trained IPO-Net and G-3DG models, as well as the progressive Gaussian cache module, enabling robust relative pose estimation and fast scene reconstruction from image observations without prior poses. We incorporate a deferred back-propagation mechanism for high-resolution training and inference, overcoming GPU memory limitations. GGRt achieves impressive inferencing and real-time rendering speeds, outperforming existing pose-free techniques and approaching pose-based 3D-GS methods. Extensive experimentation on diverse datasets confirms its effectiveness.

References

1. Bian, W., Wang, Z., Li, K., Bian, J.W., Prisacariu, V.A.: Nope-nerf: Optimising neural radiance field with no pose prior. In: CVPR. pp. 4160–4169 (2023) [3](#)
2. Charatan, D., Li, S., Tagliasacchi, A., Sitzmann, V.: pixelsplat: 3d gaussian splats from image pairs for scalable generalizable 3d reconstruction. In: CVPR (2024) [2](#), [3](#), [6](#), [10](#)
3. Chen, Y., Lee, G.H.: Dbarf: Deep bundle-adjusting generalizable neural radiance fields. In: CVPR. pp. 24–34 (2023) [4](#), [9](#), [10](#)
4. Fu, Y., De Mello, S., Li, X., Kulkarni, A., Kautz, J., Wang, X., Liu, S.: 3d reconstruction with generalizable neural fields using scene priors. In: ICLR (2024) [3](#)
5. Fu, Y., Liu, S., Kulkarni, A., Kautz, J., Efros, A.A., Wang, X.: Colmap-free 3d gaussian splatting. In: CVPR (2024) [4](#)
6. Geiger, A., Lenz, P., Urtasun, R.: Are we ready for autonomous driving? the kitti vision benchmark suite pp. 3354–3361 (2012) [9](#), [10](#), [12](#)
7. Godard, C., Mac Aodha, O., Firman, M., Brostow, G.J.: Digging into self-supervised monocular depth estimation. In: Proceedings of the IEEE/CVF international conference on computer vision. pp. 3828–3838 (2019) [7](#)
8. Gu, X., Yuan, W., Dai, Z., Tang, C., Zhu, S., Tan, P.: DRO: Deep recurrent optimizer for video to depth. IEEE Robotics and Automation Letters **8**(5), 2844–2851 (2023) [7](#)
9. Hong, S., Jung, J., Shin, H., Yang, J., Kim, S., Luo, C.: Unifying correspondence, pose and nerf for pose-free novel view synthesis from stereo pairs. arXiv preprint arXiv:2312.07246 (2023) [2](#)
10. Hong, Y., Zhang, K., Gu, J., Bi, S., Zhou, Y., Liu, D., Liu, F., Sunkavalli, K., Bui, T., Tan, H.: Lrm: Large reconstruction model for single image to 3d. In: ICLR (2024) [3](#), [4](#)
11. Kerbl, B., Kopanas, G., Leimkühler, T., Drettakis, G.: 3d gaussian splatting for real-time radiance field rendering. ACM TOG **42**(4) (2023) [1](#)
12. Lai, Z., Liu, S., Efros, A.A., Wang, X.: Video autoencoder: self-supervised disentanglement of static 3d structure and motion. In: ICCV. pp. 9730–9740 (2021) [2](#), [4](#), [10](#)
13. Li, J., Tan, H., Zhang, K., Xu, Z., Luan, F., Xu, Y., Hong, Y., Sunkavalli, K., Shakhnarovich, G., Bi, S.: Instant3d: Fast text-to-3d with sparse-view generation and large reconstruction model. In: ICLR (2024) [3](#)
14. Lin, C.H., Ma, W.C., Torralba, A., Lucey, S.: Barf: Bundle-adjusting neural radiance fields. In: ICCV. pp. 5741–5751 (2021) [3](#)
15. Liu, Y., Peng, S., Liu, L., Wang, Q., Wang, P., Theobalt, C., Zhou, X., Wang, W.: Neural rays for occlusion-aware image-based rendering. In: CVPR. pp. 7824–7833 (2022) [3](#)
16. Meuleman, A., Liu, Y.L., Gao, C., Huang, J.B., Kim, C., Kim, M.H., Kopf, J.: Progressively optimized local radiance fields for robust view synthesis. In: CVPR. pp. 16539–16548 (2023) [4](#)
17. Mildenhall, B., Srinivasan, P.P., Ortiz-Cayon, R., Kalantari, N.K., Ramamoorthi, R., Ng, R., Kar, A.: Local light field fusion: Practical view synthesis with prescriptive sampling guidelines. ACM TOG **38**(4), 1–14 (2019) [9](#), [10](#), [11](#), [13](#), [14](#)
18. Mildenhall, B., Srinivasan, P.P., Tancik, M., Barron, J.T., Ramamoorthi, R., Ng, R.: Nerf: Representing scenes as neural radiance fields for view synthesis. Communications of the ACM **65**(1), 99–106 (2021) [1](#), [3](#)

19. Sajjadi, M.S.M., Meyer, H., Pot, E., Bergmann, U., Greff, K., Radwan, N., Vora, S., Lucic, M., Duckworth, D., Dosovitskiy, A., Uszkoreit, J., Funkhouser, T., Tagliasacchi, A.: Scene Representation Transformer: Geometry-Free Novel View Synthesis Through Set-Latent Scene Representations. In: CVPR (2022) [4](#)
20. Sajjadi, M.S., Mahendran, A., Kipf, T., Pot, E., Duckworth, D., Lučić, M., Greff, K.: Rust: Latent neural scene representations from unposed imagery. In: CVPR. pp. 17297–17306 (2023) [2](#), [4](#), [10](#)
21. Sitzmann, V., Rezkikov, S., Freeman, B., Tenenbaum, J., Durand, F.: Light field networks: Neural scene representations with single-evaluation rendering. *Advances in Neural Information Processing Systems* **34**, 19313–19325 (2021) [3](#)
22. Smith, C., Du, Y., Tewari, A., Sitzmann, V.: Flowcam: Training generalizable 3d radiance fields without camera poses via pixel-aligned scene flow. In: NeurIPS (2023) [4](#), [10](#)
23. Suhail, M., Esteves, C., Sigal, L., Makadia, A.: Light field neural rendering. In: CVPR. pp. 8269–8279 (2022) [3](#)
24. Sun, P., Kretschmar, H., Dotiwalla, X., Chouard, A., Patnaik, V., Tsui, P., Guo, J., Zhou, Y., Chai, Y., Caine, B., Vasudevan, V., Han, W., Ngiam, J., Zhao, H., Timofeev, A., Ettinger, S., Krivokon, M., Gao, A., Joshi, A., Zhang, Y., Shlens, J., Chen, Z., Anguelov, D.: Scalability in perception for autonomous driving: Waymo open dataset. In: CVPR (June 2020) [9](#), [10](#), [12](#)
25. Teed, Z., Deng, J.: Raft: Recurrent all-pairs field transforms for optical flow. In: ECCV. pp. 402–419. Springer (2020) [5](#)
26. Tian, F., Du, S., Duan, Y.: Mononerf: Learning a generalizable dynamic radiance field from monocular videos. In: ICCV. pp. 17903–17913 (2023) [2](#), [4](#)
27. Wang, P., Chen, X., Chen, T., Venugopalan, S., Wang, Z., et al.: Is attention all nerf needs? In: ICLR (2023) [2](#), [3](#)
28. Wang, P., Tan, H., Bi, S., Xu, Y., Luan, F., Sunkavalli, K., Wang, W., Xu, Z., Zhang, K.: Pflrm: Pose-free large reconstruction model for joint pose and shape prediction. In: ICLR (2024) [4](#)
29. Wang, Q., Wang, Z., Genova, K., Srinivasan, P.P., Zhou, H., Barron, J.T., Martin-Brualla, R., Snavely, N., Funkhouser, T.: IBRNet: Learning multi-view image-based rendering. In: CVPR. pp. 4690–4699 (2021) [10](#)
30. Wang, Z., Bovik, A.C., Sheikh, H.R., Simoncelli, E.P.: Image quality assessment: from error visibility to structural similarity. *IEEE TIP* **13**(4), 600–612 (2004) [9](#)
31. Wang, Z., Wu, S., Xie, W., Chen, M., Prisacariu, V.A.: Nerf-: Neural radiance fields without known camera parameters. arXiv preprint arXiv:2102.07064 (2021) [3](#)
32. Yao, Y., Luo, Z., Li, S., Fang, T., Quan, L.: Mvsnet: Depth inference for unstructured multi-view stereo. In: ECCV. pp. 767–783 (2018) [3](#)
33. Yen-Chen, L., Florence, P., Barron, J.T., Rodriguez, A., Isola, P., Lin, T.Y.: iNeRF: Inverting neural radiance fields for pose estimation. In: IROS. pp. 1323–1330. IEEE (2021) [3](#)
34. Yu, A., Ye, V., Tancik, M., Kanazawa, A.: pixelNeRF: Neural radiance fields from one or few images. In: CVPR. pp. 4578–4587 (2021) [3](#)
35. Zhang, K., Kolkin, N., Bi, S., Luan, F., Xu, Z., Shechtman, E., Snavely, N.: Arf: Artistic radiance fields. In: ECCV. pp. 717–733. Springer (2022) [8](#)
36. Zhang, R., Isola, P., Efros, A.A., Shechtman, E., Wang, O.: The unreasonable effectiveness of deep features as a perceptual metric. In: CVPR. pp. 586–595 (2018) [9](#)